Flutter prediction of the benchmark supercritical wing

By H. Yu, S. T. Bose AND P. Moin

This article presents transonic aeroelastic simulation results of two-dimensional airfoils and three-dimensional wings. A series of direct numerical simulations (DNS) of forced pitching of the NACA 0012 airfoil at $Re_\infty = 10,000$ and various freestream Mach numbers, pitching frequencies, and amplitudes is performed first as solver validations, and the energy map is constructed to give insight into the free flutter boundary. The results show quantitative agreement with reference literature and confirm that the lambda shock-induced flow separation is the primary energy extraction mechanism for this two-dimensional transonic flutter. The three-dimensional configuration of interest is the NASA benchmark supercritical wing (BSCW), a focus of AIAA Aeroelastic Prediction Workshops (AePW). Forced pitching oscillation simulations (Case #1, 2$^{\text{nd}}$ AePW) are conducted using wall-modeled large-eddy simulations (WMLES). The pressure coefficient on the wing surface and its frequency response with respect to the pitching angle show excellent agreement with experiments.

1. Introduction

Aeroelasticity is a critical consideration in modern aircraft design and operation. In addition to the formation of leading-edge and tip vortices, the coupling between aerodynamic loads and structural dynamics is intensified by compressibility effects in the transonic regime. Shock-turbulent boundary layer interactions and the resulting flow separation and shock buffet amplify unsteady loads, leading to a more profound energy extraction mechanism and easier flutter onset. This phenomenon is commonly referred to as the transonic dip (Mykytow 1977), where the dynamic pressure required for flutter onset is markedly lower in the transonic region. Such flutter may result in periodic pitching or yawing oscillations that threaten structural integrity. Consequently, accurate prediction of flutter boundaries remains an important topic for both academia and industry.

This study explores computational approaches for predicting transonic aeroelasticity. This task has been a central focus of recent AIAA Aeroelastic Prediction Workshops (AePWs), mostly with unsteady Reynolds-averaged Navier-Stokes (URANS) simulations with varying turbulence models, wall functions, and numerical schemes. While the URANS results generally align with the experimental data for attached flow cases, significant data scattering among participating teams was reported for separated flow cases (Schuster *et al.* 2012; Heeg *et al.* 2016). This article explores the possibility of using wall-modeled large-eddy simulation (WMLES) as a possible higher-fidelity paradigm for transonic aeroelastic simulations.

The code charLES with Voronoi diagram-based unstructured grid is used in this article. Quasi-two-dimensional (spanwise-symmetric three-dimensional) direct numerical simulations (DNS) of the NACA0012 airfoil at $Re_c = 10,000$ are first conducted as a validation of the moving mesh solver. The results are compared to recent DNS studies with

a sharp-interface immersed boundary method (Turner *et al.* 2023, 2024*a*,*b*, 2025). An ensemble of forced pitching oscillation simulations over a range of freestream Mach numbers Ma_∞, pitch frequency f, and amplitude A is conducted. The energy map (Menon & Mittal 2019; Turner *et al.* 2024*b*) (i.e., net energy transfer per forced oscillation cycle) is constructed with polynomial interpolation in the parameter space of (Ma_∞, f, A), and the zero isosurface of the energy map is computed as the predicted limit cycle oscillation (LCO) surface. The results agree well with the reference literature by Turner *et al.* (2024*b*).

The three-dimensional configuration of interest is NASA's benchmark supercritical wing (BSCW), the focus of AePW (Schuster *et al.* 2012; Heeg *et al.* 2016) with abundant experimental data (Bennett *et al.* 1991; Dansberry *et al.* 1993; Heeg & Piatak 2013). The BSCW features a NASA SC(2)-0414 airfoil and a rectangular planform with a low aspect ratio of 2, supported by a splitter plate at the wing root. The short aspect ratio leads to a greater spanwise pressure gradient and stronger tip vortices, and these characteristics in turn give rise to buffet and flutter behaviors distinct from those of a two-dimensional airfoil. The "benign" forced pitching oscillation case (Case #1, 2$^{\text{nd}}$ AePW) is simulated with WMLES. The pressure coefficients C_p on the wing surface and their frequency response show excellent agreement with both reference literature and URANS results from participating teams. This case provides an initial assessment of the approach and a structured basis for future investigations.

The remainder of this brief is organized as follows. Section 2 describes the numerical framework and solver. The simulation setup and results for the forced pitching oscillation NACA 0012 and BSCW cases are presented in Sections 3 and 4, respectively. Section 5 summarizes the key findings and outlines directions for future work.

2. Numerical setup

This study employs the GPU-accelerated, Voronoi diagram-based unstructured finite volume solver charLES (see Brès *et al.* (2018) for details). Specifically, the compressible version of charLES with the equation of state for the ideal gas is used for all simulations. The code solves the filtered compressible Navier-Stokes equations

$$\frac{\partial \overline{\rho}}{\partial t} + \frac{\partial \overline{\rho}\tilde{u}_i}{\partial x_i} = 0, \tag{2.1}$$

$$\frac{\partial \overline{\rho}\tilde{u}_i}{\partial t} + \frac{\partial \overline{\rho}\tilde{u}_i\tilde{u}_i}{\partial x_i} = -\frac{\partial \overline{p}}{\partial x_i} + \frac{\partial \tilde{\tau}_{ij}}{\partial x_i} - \frac{\partial \tilde{\tau}_{ij}^{sgs}}{\partial x_i}, \tag{2.2}$$

$$\frac{\partial \overline{E}}{\partial t} + \frac{\partial \tilde{u}_i\overline{E}}{\partial x_i} + \frac{\partial \tilde{u}_i\overline{p}}{\partial x_i} = \frac{\partial \tilde{\tau}_{ij}\tilde{u}_i}{\partial x_i} - \frac{\partial \tilde{\tau}_{ij}^{sgs}\tilde{u}_i}{\partial x_i} + \frac{\partial}{\partial x_i}\left(\lambda\frac{\partial \overline{T}}{\partial x_i}\right) - \frac{\partial \tilde{Q}_i^{sgs}}{\partial x_i}, \tag{2.3}$$

where $\overline{(\cdot)}$ and $\tilde{(\cdot)}$ denote the filtered and Favre-filtered quantities, respectively. $\tilde{\tau}_{ij}^{sgs}$ and $\tilde{Q}_i^{sgs}$ are the subgrid stress and heat fluxes from the Vreman model Vreman (2004) or the dynamic Smagorinsky model (Germano *et al.* 1991; Lilly 1992). The equilibrium wall model (Lehmkuhl *et al.* 2018) can be employed to compute the wall shear stress for the turbulent boundary layer at a reasonable computational cost. The solver uses a second-order entropy-preserving skew-symmetric differential operator in isentropic regions for convection fluxes, and the temporal integration is achieved with a five-stage explicit Runge-Kutta scheme. The details of the solver are presented in (Brès *et al.* 2018). The subgrid and wall models can be turned off for DNS, provided that the grid is fine down

to Kolmogorov length scales and down to the viscous sublayer in near-wall regions. A moving (sliding) mesh version of charLES (see (Brès *et al.* 2023, 2025))is available and will be used when needed.

3. Forced pitching of two-dimensional airfoils

A series of quasi-two-dimensional DNS is performed for the NACA0012 airfoil undergoing prescribed forced pitching oscillation for solver validation, and the results are compared against recent two-dimensional DNS results with a sharp interface immersed boundary method (Turner *et al.* 2023, 2024*b*). The airfoil has a chord length c, and a short spanwise extent $b = 0.1c$ is used with the slip-wall boundary condition on the two spanwise domain boundaries. Voronoi diagram-based unstructured grids are used. Hexagonal close-packed (HCP) lattices are used in the farfield. While in near-wall regions, anisotropic stranded layers with a maximum aspect ratio of 4 are used to provide higher resolutions in the wall-normal direction. For the results reported in this brief, there are 320 points per chord length in the streamwise and spanwise directions, with 2.5 million control volumes in total. The results from the coarser mesh show similar results and are omitted from this brief.

An ensemble of forced pitching simulations was conducted. The pitching axis is located at the midchord $X_e = 0.5c$ (midchord). The location of the anchor point has a significant effect on the energy exchange between the fluid and structure in two-dimensional setups, as demonstrated by Turner *et al.* (2024*a*) and Menon & Mittal (2019). The present choice ensures consistency with the reference study (Turner *et al.* 2024*b*).

All quantities are nondimensionalized by the chord length c, freestream velocity U_∞, and the convection time unit c/U_∞. The non-dimensional parameters are denoted by the star superscript. The prescribed pitch motion is

$$\theta^\star(t^\star) = A\sin(2\pi f^\star t^\star), \tag{3.1}$$

where $f^\star$ is the frequency and A is the amplitude. $U^\star = 1/f^\star$ is the reduced velocity that characterizes the inflow dynamic pressure with respect to the flutter dynamic pressure. The freestream Reynolds number based on chord length $Re_\infty = U_\infty c/\nu = 10{,}000$. The parameter space of the ensemble is a tensor product of various Ma_∞, $U^\star$, and A values matching the transonic DNS reference literature (Turner *et al.* 2024*b*).

3.1. *Results and discussion*

The energy map approach (Menon & Mittal 2019; Turner *et al.* 2024*b*) is employed to analyze the ensemble of simulations with varying Ma_∞, $U^\star$, and A, providing insight into the LCO characteristics of free flutter. The nondimensional energy extraction per forced pitching period, $E^\star$, is computed by integrating the power coefficient $C_W(t^\star)$ over N forced pitching cycles of time $t^\star \in [t_0^\star,\, t_0^\star + NU^\star]$

$$E^\star = \frac{1}{N}\int_{t_0^\star}^{t_0^\star+NU^\star} C_W(t^\star)\,\mathrm{d}t^\star, \tag{3.2}$$

where $C_W = C_M(t^\star)\,\dot{\theta}^\star(t^\star)$ is the power coefficient, and $C_M = 2M/\rho_\infty U_\infty^2 c^2 b$ is the moment coefficient where M is the moment (from pressure and viscous forces) with respect to the pitching axis. The trapezoidal rule is used for numerical quadrature over $N = 10$ pitching cycles.

The computed values of $E^\star$ span the parameter space $(Ma_\infty, f^\star, A)$ across the typical

transonic region. The zero isosurface of $E^\star$ is extracted through three-dimensional polynomial interpolation of data points in the simulation ensemble. The zero isosurface of $E^\star$ corresponds closely to the bifurcation diagram of LCO flutter. Under the assumption of a harmonic LCO, the state $(Ma_\infty, f^\star, A)$ of free flutter lies on the zero isosurface, while the negative or positive signs of $\mathrm{d}E^\star/\mathrm{d}A$ indicate stable or unstable LCO, respectively.

Figure 1(a) presents the three-dimensional zero isosurface of $E^\star$, where the blue and red regions represent stable ($\mathrm{d}E^\star/\mathrm{d}A < 0$) and unstable ($\mathrm{d}E^\star/\mathrm{d}A > 0$) subsurfaces, respectively. Figure 1(b) shows the projection of the stable surface onto the (Ma_∞, $U^\star$) plane, providing a clearer visualization of the predicted flutter boundary. The results qualitatively agree with those of Turner *et al.* (2024*b*), showing stable transonic flutter up to $Ma_\infty \approx 0.76$. The projected region exhibits a reduction in $U^\star$ between $Ma_\infty = 0.67$ and 0.73, centered around 0.70. This finding is consistent with the transonic dip phenomenon, where the dynamic pressure required for flutter onset decreases in the transonic regime.

Figure 1(d) shows a slice of $E^\star$ at $f^\star = 0.1078$, illustrating the predicted transonic dip characterized by the sudden appearance of positive $E^\star$ within $0.65 \leq Ma_\infty \leq 0.75$. Figure 1(c) shows another slice at the center of the dip ($Ma_\infty = 0.70$), where positive $E^\star$ values emerge at a lower reduced velocity (higher fc/U_∞). Unlike the results obtained by Turner *et al.* (2024*b*), however, no distinct upper limit of reduced velocity for the flutter boundary is observed here.

Turner *et al.* (2024*b*) attribute the transonic dip under this specific configuration primarily to lambda shock induced flow separation and stall. Based on the dip observed in Figure 1(d), three representative cases are selected with identical reduced velocity $U^\star = 10.0$; amplitude $A = 10.0°$; and different Mach numbers $Ma_\infty = 0.6$, 0.7, and 0.8 to examine the flow dynamics across the transonic dip in detail.

Figure 2 illustrates the results at $Ma_\infty = 0.7$, corresponding to the center of the predicted transonic dip and exhibiting the largest positive $E^\star$. Figure 2(a) presents the histories of the moment and power coefficients during one pitching cycle, along with the space-time map of the surface pressure coefficient C_p at midspan on the upper surface. Four characteristic phases in the pitching cycle are identified based on the history of C_W and are marked in Figure 2(a). The corresponding snapshots of density gradient magnitude $|\nabla\rho|$ and vorticity fields are shown in Figure 2(b–e) and Figure 2(f–i), respectively. A lambda shock forms near $x/c = 0.5$ on the upper surface as the airfoil pitches up and propagates upstream, as shown in the $|\nabla\rho|$ field and indicated in the C_p contour. The associated adverse pressure gradient causes boundary layer separation near midchord, and the resulting stall vortex is shed downstream, coinciding with the sharp drop in C_M and peak energy extraction indicated by C_W. The mechanism closely agrees with the literature (Turner *et al.* 2024*b*) in terms of the timing and maximum value of peak C_W.

Figure 3 shows the corresponding data for $Ma_\infty = 0.60$. The history of C_M remains approximately in phase with the motion angle θ, without the distinct drop observed in the transonic case. Consequently, the strong energy-extraction mechanism associated with shock-induced separation is absent. The vortex shedding near midchord during the downstroke induces only small fluctuations in C_M and C_W, which do not contribute significantly to the overall energy exchange.

Figure 4 presents the results at $Ma_\infty = 0.80$. In this case, the lambda shock forms further downstream, and the separation vortices move toward the trailing edge. The motion of the lambda shock and associated vortex shedding are marked in the C_p map in Figure 4(a). Compared with $Ma_\infty = 0.70$, the flow separation exerts a weaker influence

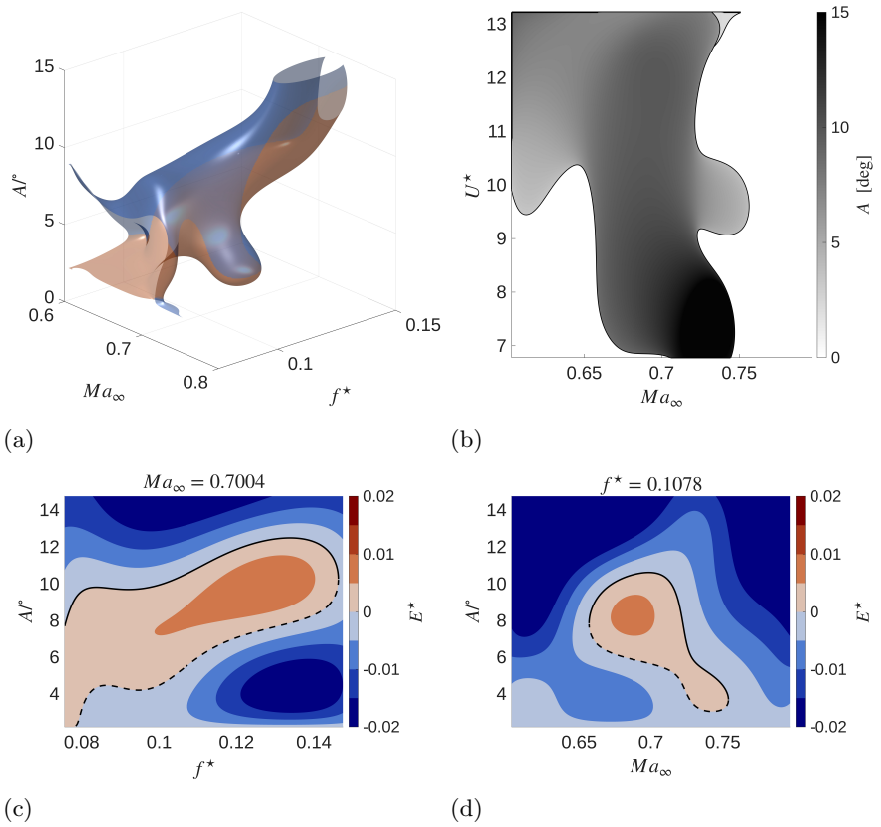

Figure 1: (a) Zero isosurface of the energy transfer map. (b) Its projection to the (Ma_∞, $U_\infty f/c$) plane, indicating the zone of stable harmonic LCOs, where the color refers to the amplitude. (c–d) Slices of the energy map at (c) fixed Ma_∞ and (d) induced frequency fc/U_∞. Solid and dashed lines represent the stable and unstable LCO boundaries, respectively.

on the moment coefficient, and C_M remains nearly in phase with θ, showing little evidence of net energy extraction.

4. Forced oscillation of a three-dimensional wing

Preliminary three-dimensional WMLES were performed for the BSCW, a configuration that has been extensively studied experimentally in the NASA Transonic Dynamics Tunnel (TDT). The BSCW features a NASA SC(2)-0414 airfoil with a chord length of 16 inches and a rectangular platform with a span of 32 inches. At the wing root, it is supported by a splitter plate. The geometry is illustrated in Figure 5. The BSCW model has been tested under two experimental configurations: the oscillating turntable (OTT) mount (Heeg & Piatak 2013), used for static and forced pitching experiments, and the pitch-and-plunge apparatus (PAPA), used for two-degree-of-freedom flutter onset prediction (Bennett *et al.* 1991; Dansberry *et al.* 1993). Similar setups have served as benchmark cases in past and ongoing AePWs (Heeg *et al.* 2016).

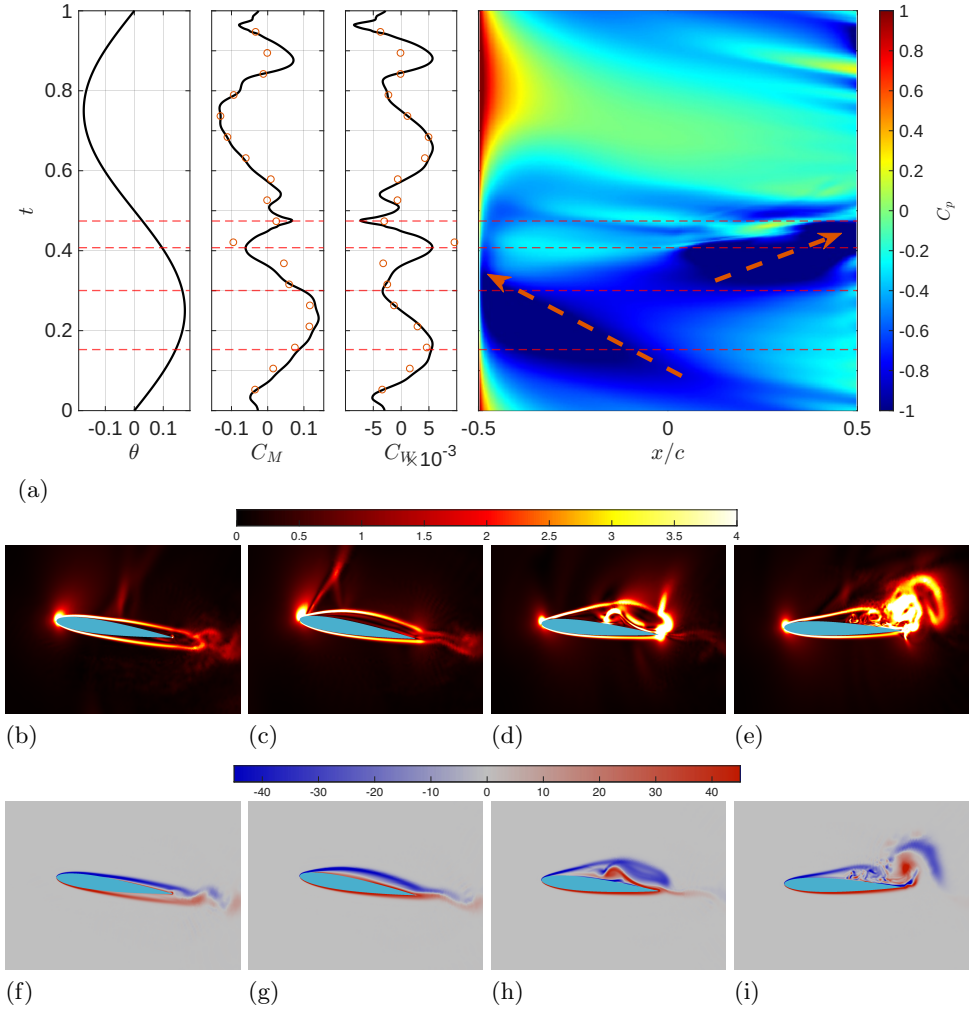

Figure 2: (a) History of angle, moment, and power coefficients for one typical forced pitching cycle and the space-time plots of the pressure coefficients on the airfoil in the same cycle under $Ma_\infty = 0.70$. Circle markers represent two-dimensional DNS results (Turner *et al.* 2023). The shock and separation regions are marked with dashed lines and circles. Four typical instances are selected and marked with dashed lines. (b–e) Density gradient magnitude, normalized by ρ_∞ and c. (f–i) Vorticity, normalized by U_∞ and c.

The present simulations focus on forced pitching oscillation Case #1 from the 2$^{\text{nd}}$ AePW (Heeg *et al.* 2016). In this case, the model is pitched about an axis located at $x/c = 0.3$ with a frequency of $f = 10$ Hz (corresponding to $St = 0.0302756716$ based on convection time unit) and an amplitude of $A = 1°$. The freestream $Ma_\infty = 0.7$ and the mean AoA 3°. Details of flow condition can be found in (Heeg *et al.* 2015, 2016). These values correspond to the attached-flow state where the transonic shock at $x/c \approx 0.1$ does not induce apparent separation. This condition serves as a less challenging case in the AePW. The experimental results are summarized in (Heeg & Piatak 2013).

Two sets of Voronoi diagram-based unstructured grids, with HCP lattices in the farfield

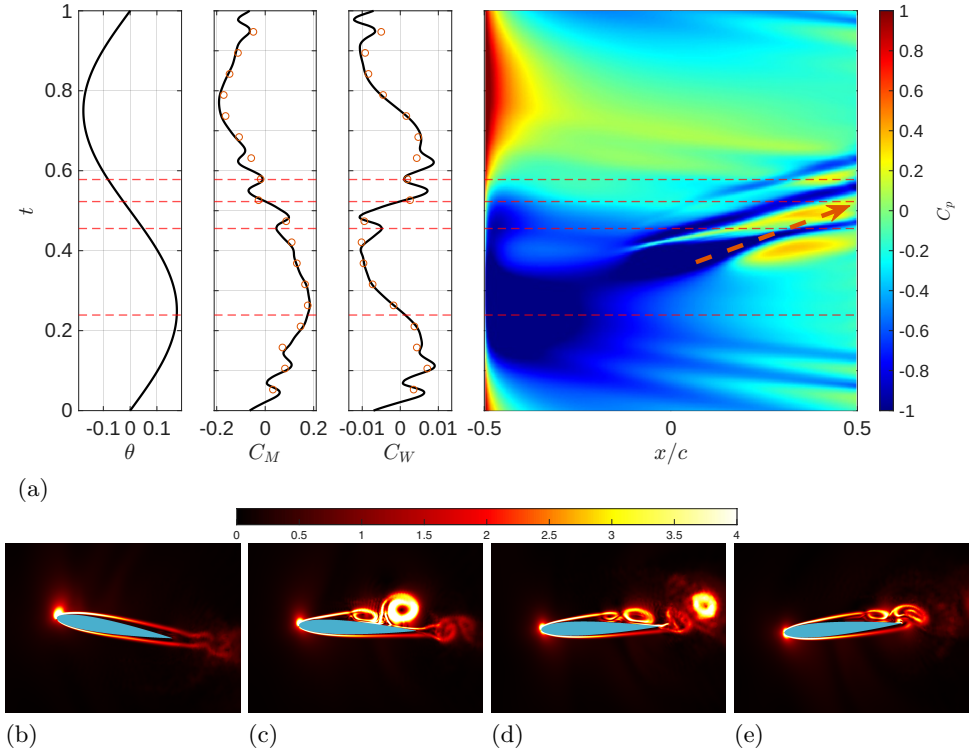

Figure 3: Similar plots for $Ma_\infty = 0.60$. The leading-edge vortex release is marked in the space-time plots. Four typical instances are selected and marked with dashed lines. (b–e) Density gradient magnitude, normalized by ρ_∞ and c.

and stranded layers of the maximum aspect ratio 4 near the wall, are employed The coarser grid, denoted by L8-L10, contains approximately 256 points per chord length in both the streamwise and spanwise directions, while the finer grid, denoted by L9-L11, contains 512 points per chord length. The Vreman subgrid model (Vreman 2004) and the equilibrium wall model (Lehmkuhl *et al.* 2018) are used.

The pressure coefficient response, C_p, is shown in Figure 6, along with comparisons with the URANS results by Chwalowski & Heeg (2016) with FUN3D and experimental data by Heeg & Piatak (2013). The mean C_p distributions on the upper and lower surfaces (Figure 6(b)(d)) agree well with the URANS predictions from other participating teams (Heeg *et al.* 2016). The discrepancy with experimental data may be attributed to the pressure transducer setup as discussed in (Heeg *et al.* 2016).

The single frequency response of C_p to the pitching motion is analyzed using the frequency response function (FRF). The magnitudes of the FRF are presented in Figure 6(b)(e), and the phases are shown in Figure 6(c)(f). Overall agreement is observed, except for a phase deviation on the upper surface near $x/c = 0.9$, where the present WMLES and URANS predict a maximum phase lag of approximately $-140°$ relative to the pitch angle, compared with $-60°$ in the experiments.

To examine this difference, we computed the spectral coherence between C_p and the pitching angle θ (Figure 7(a)(c)). The coherence decreases markedly closer to the trailing edge, indicating increased stochasticity and nonlinearity in the pressure response against

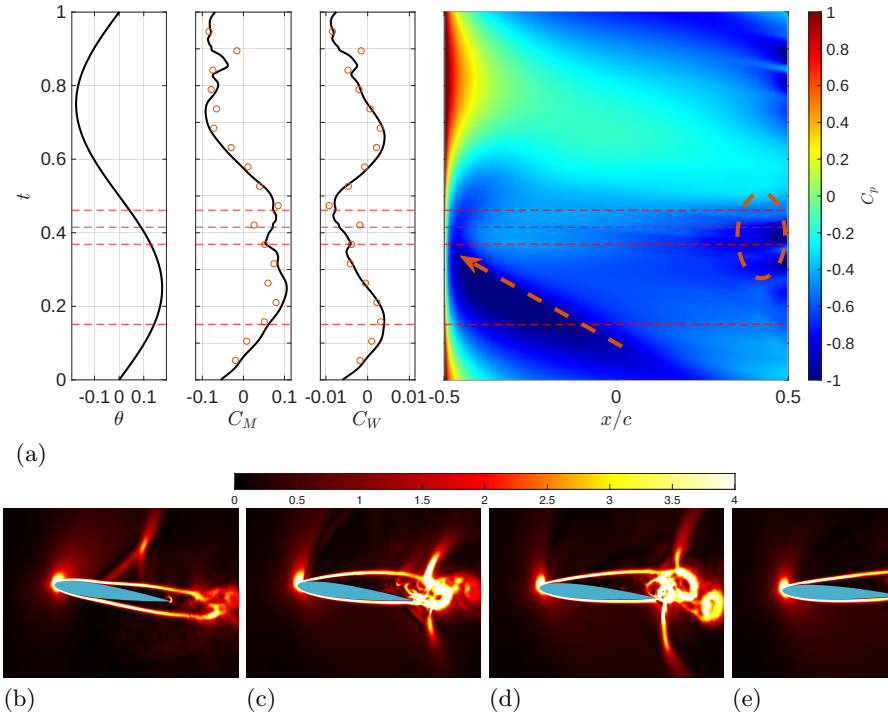

Figure 4: Similar plots for $Ma_\infty = 0.80$. The traveling of the oblique branch of the moving shock and the separation vortices at the trailing edge is shown in the space-time plots of C_p. Four typical instances are selected and marked with dashed lines. (b–e) Density gradient magnitude, normalized by ρ_∞ and c.

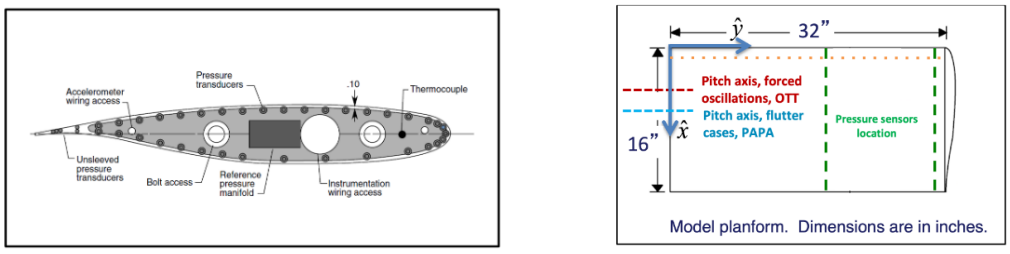

Figure 5: (a) Airfoil with experimental instruments. (b) The rectangle platform.

the angle. This might lead to a decreased confidence level of the FRF calculated. Figure 7(b)(d) shows the space-time plots of the C_p fluctuation on the upper and lower surfaces, and the two peaks of FRF magnitude (see Figure 6(b)) near the leading edges are marked by dashed lines. These peaks correspond to flow acceleration and the motion of the shock.

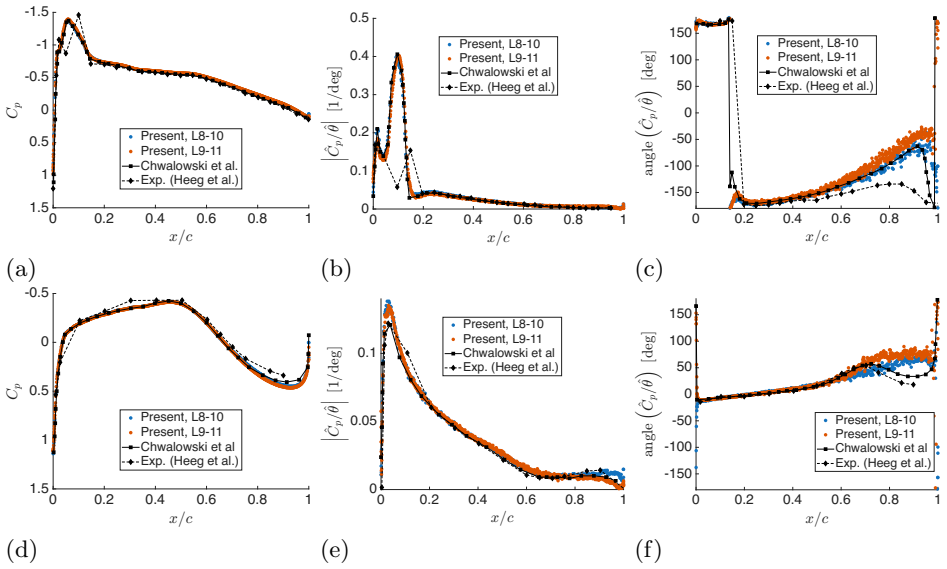

Figure 6: The response of pressure coefficient at 60% span for AePW2 Case 1. (a) Mean pressure coefficients, (b) magnitude of the frequency response function (FRF) of C_p with respect to the forced pitching, and (c) the phase angle of the FRF on the upper surface. (d–f) The same plots for the lower surface.

5. Conclusions and future work

Quasi-two-dimensional DNS were performed for the forced pitching oscillation NACA 0012 airfoil to validate the moving mesh solver based on the Voronoi diagram-based unstructured grid. The results were analyzed using an energy-based approach to gain insight into the flutter characteristics. The findings show good agreement with the recent DNS results with immersed boundary method Turner *et al.* (2024*b*), including the appearance of a transonic dip centered at approximately $Ma_\infty = 0.7$. The mechanism underlying this dip arises from the transonic shock induced separation near the midchord, which is consistent with the literature.

This framework was then applied to WMLES of the BSCW at transonic conditions with similar forced pitching motions. The freestream Mach number and mean angle of attack were selected to ensure attached flow. The predicted unsteady pressure response to the pitching motion showed good agreement with previous URANS results for both L8-L10 and finer L9-L11 grids. Our results (as well as URANS results of AePW terms) show a discrepancy with experimental results in terms of mean C_p near the leading edge of the upper surface and the FRF phase angle near $x/c = 0.9$ of the upper surface. Heeg *et al.* (2016) conjectured that the experimental setup could be the reason for the discrepancy in mean C_p. The C_p and angle θ lose spectral coherence near the trailing edge, and we conjecture that a loss of correlation leads to a decreased FRF confidence level that mispredicts the FRF phase angle.

The transonic cases in AePW with separated flow are challenging, with significant data scattering among participating teams. Future work will apply the present WMLES paradigm to these cases, notably the shock buffet prediction (Case#2 of 3$^{\text{rd}}$ AePW). The forced oscillation and free flutter cases at conditions where separated flow is expected

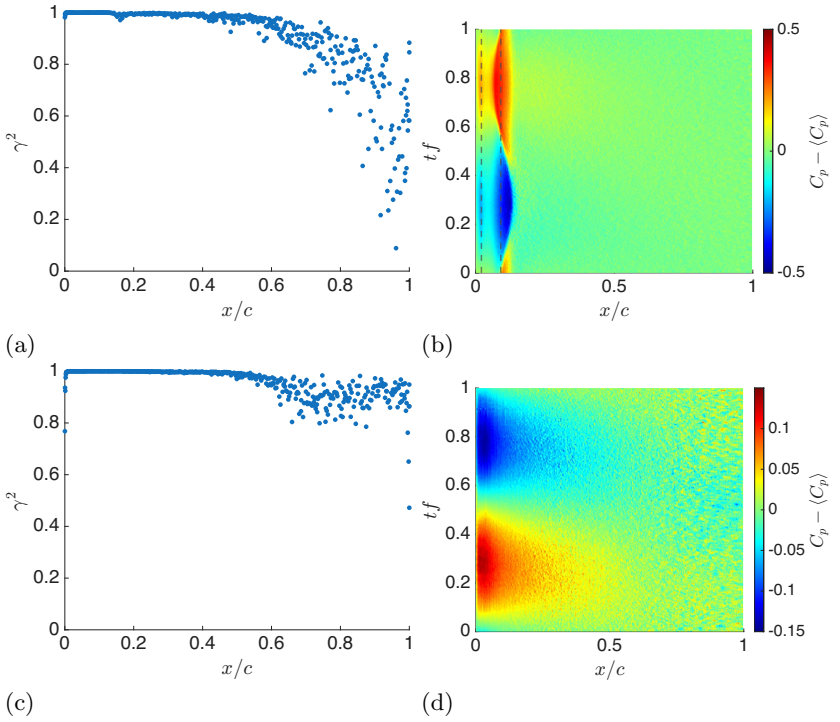

Figure 7: (a) Spectral coherence of C_p with respect to the pitch angle and (b) space-time plots of the pressure coefficient fluctuation, $C_p - \langle C_p \rangle$ on the upper surface. (c,d) The same plots for the lower surface.

will be simulated once the capability of WMLES in separated flow has been assessed in static BSCW configurations.

Acknowledgments

Support from the Office of Naval Research to the Center for Turbulence Research (grant N000142312833) is gratefully acknowledged. This research used resources of the Oak Ridge Leadership Computing Facility, which is a US Department of Energy, Office of Science, User Facility supported under contract DE-AC0500OR22725.

REFERENCES

Bennett, R., Eckstrom, C., Rivera, J., Dansberry, B., Farmer, M. & Durham, M. 1991 The Benchmark Aeroelastic Models Program—description and highlights of initial results. Tech. Rep. TM 104180, NASA.

Brès, G. A., Bose, S. T., Emory, M., Ham, F. E., Schmidt, O. T., Rigas, G. & Colonius, T. 2018 Large-eddy simulations of co-annular turbulent jet using a Voronoi-based mesh generation framework. *AIAA Paper 2018-3302* .

Brès, G. A., Wang, K., Emory, M., Ivey, C. B. & Bose, S. 2023 GPU-accelerated large-eddy simulations of the NASA fan noise source diagnostic test benchmark. In *AIAA AVIATION 2023 Forum*. San Diego, CA and Online: American Institute of Aeronautics and Astronautics.

Brès, G. A., Wang, K., Ivey, C. B., Bose, S., Okubo, G., Kamatsuchi, T. & Tanaka, H. 2025 GPU-Accelerated Large-Eddy Simulations for Aeroacoustic Predictions of a Full-Wheel Multi-Stage Turbofan Engine. In *AIAA AVIATION FORUM AND ASCEND 2025*. Las Vegas, Nevada: American Institute of Aeronautics and Astronautics.

Chwalowski, P. & Heeg, J. 2016 FUN3D analyses in support of the Second Aeroelastic Prediction Workshop. *AIAA Paper 2016-3122* .

Dansberry, B., Durham, M., Bennett, R., Rivera, J., Silva, W., Wieseman, C. & Turnock, D. 1993 Experimental unsteady pressures at flutter on the supercritical wing benchmark model. *AIAA Paper 1993-1592* .

Germano, M., Piomelli, U., Moin, P. & Cabot, W. H. 1991 A dynamic subgrid-scale eddy viscosity model. *Phys. Fluids A* **3**, 1760–1765.

Heeg, J., Chwalowski, P., Raveh, D. E., Dalenbring, M. J. & Jirasek, A. 2015 Plans and example results for the 2nd AIAA Aeroelastic Prediction Workshop. In *56th AIAA/ASCE/AHS/ASC Structures, Structural Dynamics, and Materials Conference*. Kissimmee, Florida: American Institute of Aeronautics and Astronautics.

Heeg, J., Chwalowski, P., Raveh, D. E., Jirasek, A. & Dalenbring, M. 2016 Overview and data comparisons from the 2nd Aeroelastic Prediction Workshop. *AIAA Paper 2016-3121* .

Heeg, J. & Piatak, D. J. 2013 Experimental data from the Benchmark SuperCritical Wing wind tunnel test on an oscillating turntable. *AIAA Paper 2013-1802* .

Lehmkuhl, O., Park, G. I., Bose, S. T. & Moin, P. 2018 Large-eddy simulation of practical aeronautical flows at stall conditions. *Proceedings of the Summer Program,* Center for Turbulence Research, Stanford University, pp. 87–96.

Lilly, D. K. 1992 A proposed modification of the Germano subgrid-scale closure method. *Phys. Fluids A* **4**, 633–635.

Menon, K. & Mittal, R. 2019 Flow physics and dynamics of flow-induced pitch oscillations of an airfoil. *J. Fluid Mech.* **877**, 582–613.

Mykytow, J, W. 1977 A brief overview of transonic flutter problems. Tech. Rep. AGARD-CP-226, Advisory Group for Aerospace Research and Development.

Schuster, D. M., Chwalowski, P., Heeg, J. & Wieseman, C. D. 2012 Summary of data and findings from the First Aeroelastic Prediction Workshop. In *Proceedings of the 7th International Conference on Computational Fluid Dynamics*. NASA Langley Research Center.

Turner, J., Seo, J. H. & Mittal, R. 2023 Analysis of the flow physics of transonic flutter using energy maps. *AIAA Paper 2023-0083* .

Turner, J., Seo, J. H. & Mittal, R. 2024*a* Time-accurate fluid–structure interaction (FSI) simulations of transonic flutter. *AIAA Paper 2024-1354* .

Turner, J., Seo, J.-H. & Mittal, R. 2025 Three-dimensional simulations of transonic shock-stall on a sinusoidally pitching wing. *AIAA Paper 2025-1494* .

Turner, J. M., Seo, J.-H. & Mittal, R. 2024*b* Sinusoidally pitching foils in transonic flow: insights into flutter from time accurate simulations. *AIAA J.* **62**, 1148–1158.

Vreman, A. W. 2004 An eddy-viscosity subgrid-scale model for turbulent shear flow: algebraic theory and applications. *Phys. Fluids* **16**, 3670–3681.